Acta Pharmaceutica Sinica B 2025;15(3):1255−1267

Chinese Pharmaceutical Association
Institute of Materia Medica, Chinese Academy of Medical Sciences

Acta Pharmaceutica Sinica B

www.elsevier.com/locate/apsb
www.sciencedirect.com

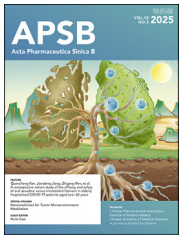

ORIGINAL ARTICLE

Disrupting calcium homeostasis and glycometabolism in engineered lipid-based pharmaceuticals propel cancer immunogenic death

Qiuxia Peng[a,b,†], Xiaolong Li[c,†], Chao Fang[a,†], Chunyan Zhu[a,b], Taixia Wang[a,b], Binxu Yin[a], Xiulin Dong[a], Huaijuan Guo[a,d], Yang Liu[a,d], Kun Zhang[a,*]

[a]*Central Laboratory and Department of Medical Ultrasound, Sichuan Academy of Medical Sciences, Sichuan Provincial People's Hospital, School of Medicine, University of Electronic Science and Technology of China, Chengdu 610072, China*
[b]*Central Laboratory and Department of Medical Ultrasound, Shanghai Tenth People's Hospital, School of Medicine, Tongji University, Shanghai 200072, China*
[c]*Department of Ultrasound, Zhongshan Hospital, Institute of Ultrasound in Medicine and Engineering, Fudan University, Shanghai 200032, China*
[d]*Department of Oncology, Affiliated Hospital of Yangzhou University, Yangzhou 225009, China*

Received 1 August 2024; received in revised form 28 October 2024; accepted 5 November 2024

KEY WORDS

Calcium homeostasis disruption;
Glycometabolism interference;
Immunogenic cell death;
Oxidative stress;
Lactic acid;
Engineered lipids;

Abstract Homeostasis and energy and substance metabolism reprogramming shape various tumor microenvironment to sustain cancer stemness, self-plasticity and treatment resistance. Aiming at them, a lipid-based pharmaceutical loaded with CaO_2 and glucose oxidase (GOx) (LipoCaO_2/GOx, LCG) has been obtained to disrupt calcium homeostasis and interfere with glycometabolism. The loaded GOx can decompose glucose into H_2O_2 and gluconic acid, thus competing with anaerobic glycolysis to hamper lactic acid (LA) secretion. The obtained gluconic acid further deprives CaO_2 to produce H_2O_2 and release Ca^{2+}, disrupting Ca^{2+} homeostasis, which synergizes with GOx-mediated glycometabolism interference to deplete glutathione (GSH) and yield reactive oxygen species (ROS). Systematical experiments reveal that these sequential multifaceted events unlocked by Ca^{2+} homeostasis disruption

*Corresponding author.
E-mail address: zhang1986kun@126.com (Kun Zhang).
†These authors made equal contributions to this work.
Peer review under the responsibility of Chinese Pharmaceutical Association and Institute of Materia Medica, Chinese Academy of Medical Sciences.

https://doi.org/10.1016/j.apsb.2024.12.018

Starvation therapy;
Cancer plasticity

and glycometabolism interference, ROS production and LA inhibition, successfully enhance cancer immunogenic deaths of breast cancer cells, hamper regulatory T cells (Tregs) infiltration and promote $CD8^+$ T recruitment, which receives a considerably-inhibited outcome against breast cancer progression. Collectively, this calcium homeostasis disruption glycometabolism interference strategy effectively combines ion interference therapy with starvation therapy to eventually evoke an effective anti-tumor immune environment, which represents in the field of biomedical research.

1. Introduction

Abnormal homeostasis, energy substance metabolism are two typical characteristics of malignant tumor[1-5], which shape various and complex tumor microenvironment to sustain cancer stemness[6], self-plasticity and treatment resistance and directly decide cancer progression and evolution[7,8]. In various types of metabolisms, glucose as the bottommost unit provides energy and substance supply to sustain the proliferation and growth of tumor cells the Warburg Effect[9,10]. Beyond that, glucose metabolism also correlates with the immune system[11,12]. Typically, lactate originating from anaerobic glycolysis of glucose can not only stimulate the proliferation and functional activation of T regulatory cells (Tregs)[13], but also inhibit immune responses and promote tumor growth[14,15]. Regarding this, targeted disrupting glycometabolism is believed to serve as a general route to engineer various starvation therapy protocols and enhance anti-tumor immune responses.

It has been extensively accepted that there are many complementary effects that contribute to the complex tumor microenvironment and tumor heterogeneity that encourage cancer progression and self-adaptation[1,3]. Therefore, only interfering in one avenue (glycometabolism) is usually inadequate to completely repress cancer[8], and multiplexed disruptions are receiving increasing attention, which hasten the birth of various combined therapies[16]. Ion homeostasis as one component of tumor homeostasis also decides cancer progression and affects immunotherapy[17-20]. Based on this rationale, the concept of ion-inference therapy has been proposed[21-24], but the study in this field is still burgeoning, let alone the combination of ion homeostasis disruption with other avenue interferences.

In this report, two avenues, calcium ion (Ca^{2+}) homeostasis disruption and glycometabolism interference, are concurrently taken into consideration and enabled in one lipid-based pharmaceutical to induce apoptosis and immunogenic cell death (ICD) of breast cancer cells and repress their progression. Therein, lipid was used as vehicles to load and encapsulate glucose oxidase (GOx) and calcium peroxide (CaO_2), obtaining LipoCaO_2/GOx (LCG) (Scheme 1). In the glycometabolism interference, depleting glucose or occluding glucose supply in tumor cells has been validated to hinder the progression of tumors[25-29]. Especially, GOx-mediated glucose consumption represents a significant advancement for tumor starvation therapy[30,31], which provides a solid foundation for glycometabolism interference using LCG. Moreover, the route, GOx-catalyzed glucose depletion, competes with anaerobic glucose glycolysis. This means that lactic acid (LA) production originating from anaerobic glucose glycolysis was expected to be dampened, and the function of Tregs in suppressing the immune system would undoubtedly be impaired (Scheme 1)[32]. Additionally, GOx-catalyzed glucose into H_2O_2 and gluconic acid, wherein H_2O_2 served as the reactive oxygen species (ROS) source and GSH scavenger to enrich ROS available for inducing ICD (Scheme 1)[11].

CaO_2 is sensitive to pH and gradually decomposes within the acidic tumor microenvironment, eventually resulting in the release of free Ca^{2+} ions and H_2O_2[33]. Inspired by it, Ca^{2+} overload in this report was expected to disrupt the inherent Ca^{2+} homeostasis, induce cancer apoptosis and enhance immune response. More significantly, both Ca^{2+} and H_2O_2 have been identified as potential inducers of ICD in tumor cells[34,35], which thereby brought about immunogenic deaths of breast cancer. Contributed by the above-multifaceted events, the direct apoptosis in combination with the enhanced ICD not only led to the direct eradication of tumor cells, but also initiated a targeted immune response against breast cancer progression (Scheme 1). Beyond LA inhibition, ROS originating from glucose and CaO_2 decomposition into H_2O_2 is also designed to disfavor Tregs recruitment and oppose the immunosuppressive tumor microenvironment, according to previous experiences (Scheme 1)[36-38]. Collectively, both Ca^{2+} homeostasis disruption and glycometabolism interference that integrated into such lipid-based pharmaceuticals provide a general candidate strategy to treat malignant tumor and guide the development of clinical translation-orientated pharmaceuticals.

2. Materials and methods

2.1. Reagents and materials

Cholesterol was purchased from Sigma−Aldrich (USA); dipalmitoylphosphatidylcholine (DPPC), PEG_{2k} conjugated distearinphosphatidylethanolamine (DSPE-mPEG_{2k}) were purchased from Meilunbio and Solarbio (China). 1,1′-Dioctadecyl-3,3,3′,3′-tetramethylindodicarbocyanine perchlorate DiIC18 was purchased from Abcam (UK). $CaCl_2$ and NaOH were purchased from Aladdin. Dulbecco's modified Eagle medium (DMEM), Phosphate buffered solution (PBS), Glucose oxidase (GOx), Trypsin Digestion solutions, 0.25% were purchased from Solarbio (China). Calcein/PI Live/Dead Viability/Cytotoxicity Assay Kit and Reactive Oxygen Species Assay Kit were purchased from Beyotime (China).

2.2. Preparation of CaO_2 nanoparticle solution

One gram of calcium chloride was dissolved in 10 mL of distilled water, followed by the addition of 5 mL of ammonia solution (1 mol/L) and 80 mL of PEG 200 to the stirring mixture. Subsequently, 5 mL of 30% H_2O_2 was added to the mix at a rate of 3 drops per minute. The preparation procedure took place in continuously stirred open glass beakers at room temperature, with

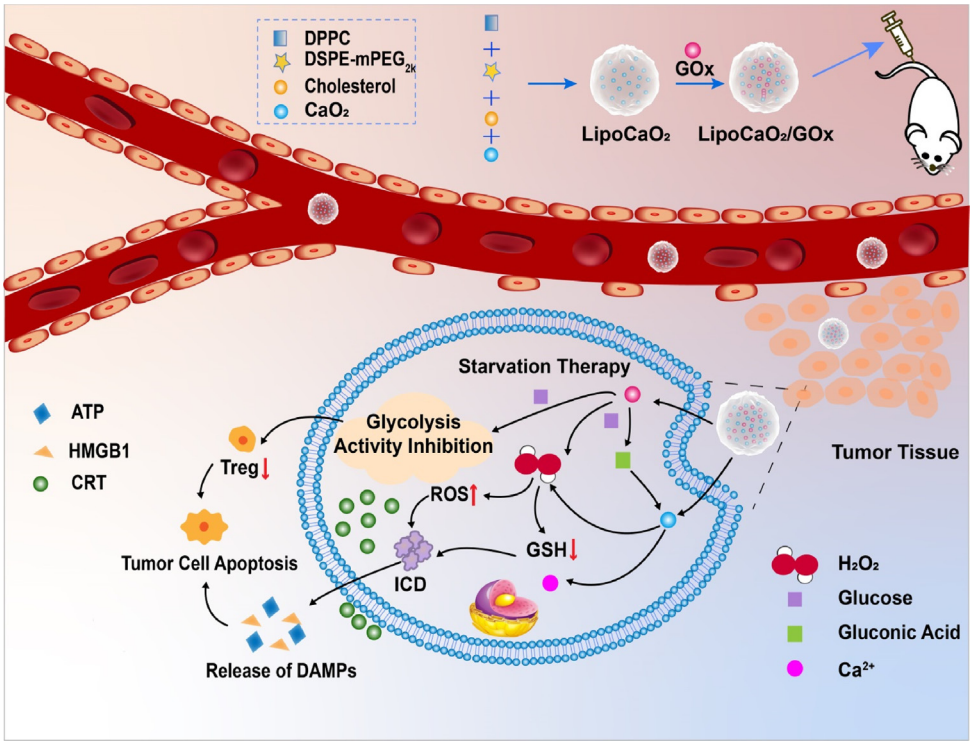

Scheme 1 Schematic diagram illustrating LCG synthesis and how the combination of calcium homeostasis and glycometabolism in LCG pharmaceuticals unlock multifaceted events hamper Tregs infiltration and function, encourage $CD8^+$ T recruitment and brought about cancer immunogenic death to repress breast cancer.

the stirrer velocity kept constant for all experiments. After 6 h of stirring, a clear and colorless to yellowish solution was obtained.

2.3. *Preparation of nanocomposites*

To prepare liposomes, a lipid mixture of DPPC, cholesterol, and DSPE-mPEG$_{2k}$ was dissolved in chloroform at a mole ratio of 8:4:1[1]. Then, 0.1 mL of CaO_2 in ethanol (10 mg/mL) was added to the mixture, followed by the formation of a thin lipid film after rotary evaporation. Subsequently, 1 mL of GOx aqueous solution (1 mg/mL) was added to the lipid film and stirred for 30 min. The mixture was then extruded through a 200 nm polycarbonate filter 20 times to obtain a uniform lipid suspension. The suspension was centrifuged at 10,000 rpm for 20 min (purchased from China Hunan Xiangyi Laboratory Instrument Development Co., Hunan, China) and the unloaded GOx supernatant was discarded. Ultrapure water was added to the precipitate to form liposomal LCG. LipoGOx (LG) and lipoCaO_2 (LC) were prepared using a similar procedure but without the addition of CaO_2 or GOx to the lipid membranes.

2.4. *Characterization of the nanoparticles*

DLS and Zeta potential were measured using a Zetasizer Nano ZS90. TEM images were captured with a JEM 1200EX. XRD patterns were obtained using a Bruker D8 Advance X-ray powder diffractometer. XPS results were obtained from an imaging X-ray photoelectron spectrometer, specifically the 250Xi model.

2.5. *pH-dependent CaO_2 release*

Confirmation of the pH dependence of CaO_2 release from LCG NPs was conducted using PBS solutions with different pH values (7.4, 6.5, and 5.5). One milliliter of LCG NPs (CaO_2 = 1 mg/mL) was added to a dialysis bag with a molecular weight cutoff (MCWO) of 3500 and immersed in 30 mL of PBS solution in a 50 mL centrifuge tube. All samples were placed in a thermostatic shaker at 37 °C and 100 rpm/min. At time points of 1, 2, 4, 8, and 12 h, 1 mL of solution was taken out for analysis.

2.6. *Catalytic ability measurement*

To assess the catalytic activity of LCG, glucose solutions of varying concentrations were treated with LCG, LG, or free GOx (10 μg/mL). The solutions were collected at different time points to measure H_2O_2 levels and pH.

2.7. *Measurement of GSH content in solution*

GSH levels were assessed using a commercially available assay kit to measure reduced glutathione content. Briefly, 10 μL of the experimental group (PBS, Liposome, etc.) was mixed with 100 μL of GSH (1 mmol/L), and 20 μL of the mixture was added to the assay reagent. The absorbance at 412 nm was then measured using an enzyme meter.

2.8. *In intracellular H_2O_2 generation*

To measure the intracellular H_2O_2 concentration of cells after different treatments, the experimental groups (PBS, Liposome, etc.) were co-incubated with the cells for 4 h. Subsequently, the cells were collected and 200 μL of Hydrogen Peroxide Detection Lysate was added, followed by sufficient homogenization to break up and lyse the cells. The supernatant was then centrifuged, hydrogen peroxide detection reagent was added, and left at room

temperature for 30 min. The absorbance of the solution at 560 nm was recorded using an enzyme counter.

2.9. In intracellular GSH depletion

To determine intracellular GSH levels, cells were cultured in 6-well plates. The cells were co-incubated with the nanoparticles (GOx = 10 μg/mL) for 4 h. Subsequently, the cells were collected and disrupted by sonication. The absorbance at 412 nm is measured finally, following the procedure for using the kit.

2.10. Measurement of LA levels

To measure intracellular levels of LA, cells were seeded in 6-well plates. The cells were then incubated with the nanomaterials (GOx = 10 μg/mL) for 4 h. Subsequently, the cells were harvested for further analysis.

2.11. Cellular uptake assay

Cells were inoculated at a density of 1×10^5 per dish in confocal dishes and cultured for 12 h. LCG-DID (GOx = 10 μg/mL) was co-incubated with the cells, followed by three washes with PBS and staining with DAPI. Confocal microscopy was used to acquire images, and subsequently, the cells were collected by trypsin digestion and analyzed using flow cytometry.

2.12. Live/dead cell staining assessment

Live and dead cell assays were utilized to validate the cytotoxicity of LCG (GOx = 10 μg/mL) on tumor cells. The cells were seeded into 12-well plates and incubated for 12 h. Subsequently, the cells were stained with Calcein AM/PI solution for 30 min, followed by observation and recording under a fluorescence microscope.

2.13. Cell apoptosis assay

Cells were inoculated into 6-well plates and incubated overnight. The cells were then co-incubated with different nanomaterials (GOx = 10 μg/mL). After incubation, the cells were collected and washed with PBS. Subsequently, detection solution was added to the cells and they were incubated at room temperature, protected from light for 20 min. Following this, the cells were placed in an ice bath and detected by flow cytometry.

2.14. Intracellular ROS and Ca^{2+} assay

Briefly, cells were inoculated into confocal dishes and incubated overnight. The cells were then co-incubated with the nanomaterials for 4 h. Subsequently, the cell culture fluid was removed, and DCFH-DA (10 μmol/L) was added and incubated in the incubator for 20 min. After incubation, the cells were washed three times with a serum-free medium, and the images were observed under confocal microscopy. Finally, the cells were collected with trypsin and used for flow cytometric analysis.

Fluo-4 AM is a cell-permeable Ca^{2+} indicator that reacts with intracellular esterase to produce non-fluorescent Fluo-4. The presence of Ca^{2+} imparts strong fluorescence to Fluo-4. To detect Ca^{2+} expression within the cells, the cells were co-cultured with the nanomaterials as described above. At the end of the incubation, the Fluo-4 staining solution was added and incubated for 30 min, protected from light. Finally, the samples were observed under a confocal microscope and images were recorded.

2.15. Detection of immunogenic cell death in vitro

4T1 cells were seeded and incubated at 37 °C for 24 h, followed by different treatments. The treated cells were collected, fixed with 4% paraformaldehyde, permeabilized with 0.25% Triton X-100, blocked with 3% BSA, and then incubated with CRT antibody overnight at 4 °C. Subsequently, the cells were incubated with FITC-labeled secondary antibodies at room temperature for 1 h. Finally, the cells were stained with DAPI and representative fluorescence images were obtained using CLSM confocal excitation.

In a separate experiment, after collecting and treating the cells as described above, they were fixed with 4% paraformaldehyde, permeabilized with 0.25% Triton X-100, blocked with 3% BSA, and then incubated overnight at 4 °C with anti-heat shock protein70 (HSP70) antibodies. Following this step, the cells were incubated with FITC-labeled secondary antibodies at room temperature for 1 h. Finally, the cells were stained with DAPI and representative fluorescence images were obtained by confocal excitation of CLSM.

Furthermore, in another set of experiments, the cells were collected and treated with 4% paraformaldehyde fixation, 0.25% Triton X-100 permeabilization, and 3% BSA blocking. The cells were then incubated with anti-HMGB1 antibodies, followed by staining with Alexa Fluor 555 coupled secondary antibodies and DAPI staining. The level of HMGB1 was detected using the CLSM method.

2.16. Intracellular ATP assay

Cells were inoculated into 6-well plates and cultured overnight. The original medium was removed, and the medium containing different materials was added for co-incubation for 4 h. Subsequently, the cells were lysed by adding a lysis solution. After lysis, centrifugation was performed at 4 °C at 12,000×*g* for 5 min. The supernatant was then removed and used for subsequent assays. Twenty microliters of sample or standard were added to the assay wells or tubes and quickly mixed with a micropipette. After a minimum interval of 2 s, the relative light units (RLU) values were determined by chemiluminescence.

2.17. Western blot assay

4T1 cells were lysed in RIPA lysis buffer containing phenyl methyl sulfonyl fluoride (PMSF) on ice for 15 min. The lysate was then centrifuged at 10,000×*g* for 5 min to obtain the protein supernatant. After quantification of the protein using a BCA protein assay kit and addition of sample loading buffer, the target proteins were separated by 12% SDS-PAGE gel and transferred to a polyvinylidene difluoride (PVDF) membrane. Subsequently, the target proteins were probed with primary antibodies against GAPDH, CRT, HMGB1, and FOXP3. Finally, the results were documented following incubation with the corresponding secondary antibodies.

2.18. Imaging and biodistribution study

BALB/c mice were injected with LCG-DID or free DID in the tail vein. Fluorescence intensity images of each mouse were collected

at different periods. The hearts, livers, spleens, lungs, and kidneys of the mice were taken at 6 and 48 h, respectively. Finally, fluorescence intensity images were collected for analysis.

2.19. *In vivo antitumor studies*

When the tumor volume of mice reached approximately 180 mm^3, mice carrying 4T1 tumors were randomly divided into five groups ($n = 5$) and injected with different nanomaterials. Glucose oxidase (GOx) was administered at a dose of 2 mg/kg on Days 7, 11, and 15 after tumor inoculation. The size of the tumors and the body weights of the mice were measured every two days following the treatments to assess therapeutic efficacy and systemic toxicity, respectively. On the Day 21 after tumor inoculation, the mice were euthanized and tumor tissues were collected for comparison, weighing, and further immunohistochemical analysis.

2.20. *Elisa assay*

In brief, mouse blood samples were centrifuged for 15 min at $1000\times g$. The upper serum was collected, and the expression levels of cytokines IFN-γ, IL-6, and TNF-α in the serum were detected using Elisa.

2.21. *Evaluation of different immune cells*

To assess the immune response induced by LCG, mouse tumors were collected after various treatments and prepared into single-cell suspensions using a mouse tumor dissociation kit (130-096-730) the suspensions were then filtered through a 70 μm mesh. Subsequently, an appropriate amount of FC block was added and incubated for 10 min at 2−8 °C in the dark. Surface antibodies, including anti-CD45, anti-CD3, anti-CD4, and anti-CD8 (purchased from Biolegend, USA), were added for co-incubation. Live and dead cell staining was performed for each group, followed by fixation and membrane permeabilization before adding anti-FOXP3. FCM was utilized to measure the quantity of $CD8^+$ T cells as well as the proportion of Treg cells. Additionally, the maturation rate of DCs in tumor tissues was assessed by flow cytometry after staining with anti-CD45, anti-CD11B, anti-CD80, and anti-CD86 (purchased from Biolegend, USA).

2.22. *Statistical analysis*

The data are presented as means ± standard deviations (SD). Statistical significance was assessed using Student's *t*-test for comparisons between the experimental and control groups (*$P < 0.05$; **$P < 0.01$; and ***$P < 0.001$).

3. Results and discussion

3.1. *Synthesis and characterizations of LCG (LipoCaO₂/GOx)*

Liposomes serve as amphiphilic carriers to simultaneously encapsulate CaO_2 and GOx, and the detailed procedures are shown in Fig. 1A, wherein the other three counterparts, Liposome, LC and LG, were also obtained. In the current study, PEG200-stabilized CaO_2 nanoparticles were firstly synthesized by reacting $CaCl_2$ with H_2O_2 in an alkaline environment[39]. Transmission electron microscopy (TEM) reveals that CaO_2 is uniformly dispersed in anhydrous ethanol solution with around 20 nm in diameter (Fig. 1B) and high crystallinity (Supporting Information Fig. S1) since typical diffraction peaks of CaO_2 at $2\theta = 30.1°$, 35.6°, and 47.3° are observed[40]. The obtained liposomes and LipoCaO_2/GOx (LCG) nanoparticles are also uniformly dispersed in the PBS (Fig. 1C and Supporting Information Fig. S2). Dynamic light scattering (DLS) measurements reveal that the hydrodynamic diameters of LCG and its intermediates (liposomes, LC, LG) reside between 100 and 200 nm (Fig. 1D), denoting the success of LCG and its intermediates. Additionally, the zeta potential of LCG and its intermediates is below −40 mV. The negatively-charged surfaces dictate that LCG can remain stable in solution (Fig. 1E and Supporting Information Fig. S3). It has been documented that H_2O erosion is accessible to CaO_2, resulting in CaO_2 decomposition and failure in inducing Ca^{2+} homeostasis disruption before they can enter cancer cells[41]. Inspiringly, liposomes encapsulation is helpful to shield CaO_2 against H_2O erosion since high crystalline of CaO_2 in LCG that experience H_2O treatment for 6 h is retained (Fig. 1F).

Furthermore, the presence of CaO_2 in LCG was validated through X-ray photoelectron spectroscopy (XPS), and no alteration in characteristic peaks at 346.39 and 531.31 eV representing Ca^{2+} and O^- unveil the successful encapsulation and stability of CaO_2 by lipids (Fig. 1G and Supporting Information Fig. S4). In addition, the presence of Ca, O, P, N and C elements is observed in the energy dispersive spectrum (EDS, Fig. 1H). All these results confirm the successful synthesis and encapsulation of CaO_2 in LCG. The liposome exhibits an absorption peak at 260 nm, while GOx shows an absorption peak at 280 nm (Fig. 1I). Subsequently, we explored the decomposition and Ca^{2+} release from LCG under different pH values. Under neutral condition, the lipid structure remains intact and only a small amount of H_2O enter the internal cavity of liposomes to react with CaO_2 and produce Ca^{2+}, which also denotes the lipid shell protection effect and the high LCG stability that is appropriate for delivery. In contrast, the rapid decomposition and release of Ca^{2+} from CaO_2 in LCG is observed in an acidic environment, and lower pH favor more CaO_2 decomposition and Ca^{2+} release (Fig. 1J), respectively. This phenomenon is attributed to that low pH value destroy lipid shell and allow more H^+ ions and H_2O molecules to touch and decompose CaO_2. Such pH-dependent structure evolution and Ca^{2+} release manipulated by lipid shell determine that LCG may maintain high stability during blood circulation and then collapse to release Ca^{2+} and GOx in acidic TME without premature breakdown for disrupting Ca^{2+} homeostasis and interfering glycometabolism.

3.2. *Enzyme activity assay*

High GOx catalytic activity is the premise of high starvation therapy outcome regulating glycometabolism. Herein, we comprehensively explored the catalytic activity of GOx in free or encapsulation sates. After incubations with glucose solution (certain concentration), free GOx, LipoGOx (LG) and LCG (GOx = 10 μg/mL) result in a decrease in pH value (Fig. 2A and B) and the increase in H_2O_2 concentration (Fig. 2C and D) in the mixed solution as the functions of incubation time and glucose concentration. The variation trends in decreasing pH value and elevating H_2O_2 concentration are identical in such three samples, and the catalytic activity of GOx in the three samples is approximately identical. These indicate that GOx in LG and LCG can effectively catalyze the conversion of glucose into gluconic acid and H_2O_2, and lipid shell is disabled to impair the catalytic capacity of GOx in LG or LCG.

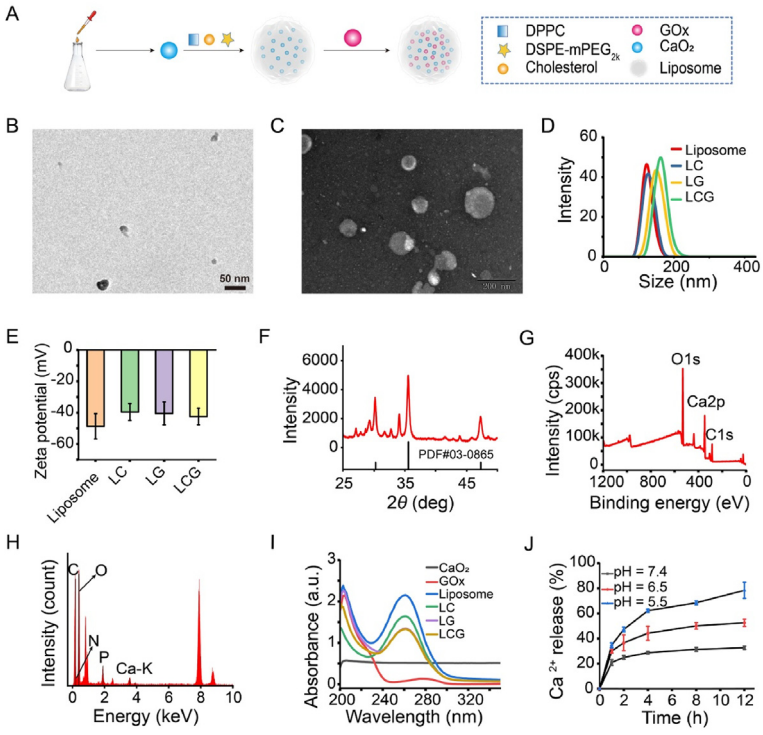

Figure 1 Construction and characterization of LCG. (A) Schematic diagram of LCG synthesis, scale bar = 50 nm; (B) TEM images of CaO_2 nanoparticles, scale bar = 20 nm; (C) TEM images of LCG nanoparticles; (D, E) Particle size distribution (D) and zeta potential (E) of different nanoparticles. (F−H) XRD (F), XPS (G) and EDS (H) spectra of LCG; (I) UV absorption spectra of different nanoparticles; (J) Ca^{2+} release from LCG at different pH conditions. Data are expressed as mean ± SD, $n = 3$.

It has been determined that the intracellular concentration of GSH in tumors is approximately up to 10 mmol/L which is 10 times higher than extracellular GSH[42]. High H_2O_2 concentration expedite GSH depletion[43]. The above experiments validate that GOx in LCG or LG can decompose glucose into gluconic acid and H_2O_2, which will deplete GSH. Actually, CaO_2 in LCG is also expected to react with H_2O and produce H_2O_2 to deplete GSH. To investigate the GSH depletion by CaO_2 in LCG, we utilized an oxidized glutathione (GSSG) test kit (DTNB) as a GSH indicator, wherein no glucose avoids GOx-mediated H_2O_2 production. The concentration of GSH is found to be directly proportional to the absorbance at 412 nm (Supporting Information Fig. S5). It exhibits a rapid decrease in both the LCG and LipoCaO_2 (LC) groups, while there is no significant change in the CaO_2-free groups including Liposome and LG groups (Fig. 2E). As the LCG concentration climbs, more GSH depletion is accessible (Fig. 2F), indicating that CaO_2 in LCG has a significant capacity to produce H_2O_2 for depleting GSH.

3.3. *Cellular-level evaluations on multifaceted actions in LCG*

Afterwards, cellular-level evaluations on how Ca^{2+} homeostasis disruption and glycometabolism interference in LCG regulate the levels of H_2O_2, ROS, GSH, pH value and Ca^{2+} were carried on. Prior to cellular-level evaluations, the cellular uptake and intracellular distribution of nanomaterials were investigated, and DID dye-labeled LCG (namely LCG-DID) was used to dye the engulfed nanoparticles since DID can emit red fluorescence under laser excitation at 633 nm. 4T1 cells were incubated with LCG-DID for 0.5, 1, 2 and 4 h, and subsequently, we evaluated the engulfment levels of LCG-DID by 4T1 cells using laser confocal scanning microscopy (LCSM) and flow cytometry (FCM). Results show the considerably-elevated phagocytosis of LCG-DID by 4T1 cells and longer incubation time harvests more LCG-DID engulfment (Fig. 3A and B and Supporting Information Fig. S6), and the entry route is found to follow the lysosome pathway (Fig. 3A). Similar phenomenon is observed in H22 cells that are one liver cancer line, where more LCG-DID nanoparticles are engulfed by H22 cells as the incubation time is prolonged (Supporting Information Figs. S7 and S8). Importantly, Ca^{2+} release only occurs within cancer cells, as evidenced by neglectable Ca^{2+} difference in the extracellular matrix after incubating with or without LCG (Fig. 3C). These results provide adequate and reliable evidence and basis to enable LCG to disrupt Ca^{2+} homeostasis and interfere glycometabolism, consequently decomposing glucose into H_2O_2, depleting GSH to produce ROS, lowering pH value and releasing Ca^{2+}.

Subsequently, we quantified the concentration of H_2O_2 in breast cancer cells treated with different samples. Contributed by the H_2O-triggered CaO_2 decomposition and GOx-mediated glucose decomposition for producing abundant ROS, a rise in intracellular H_2O_2 concentration is observed (Fig. 3D). This result indicates that LC, LG and LCG have the capability to generate abundant H_2O_2, and LCG gives birth to the most H_2O_2, which will lead to significant cytotoxicity and imposing severe oxidative stress on tumor cells. Additionally, we tracked the level of intracellular GSH in 4T1 cells treated with nanoparticles, and it was found that LC, LG and LCG have the capability to deplete GSH in 4T1 and H22 cells at the cellular level (Fig. 3E and Supporting Information Fig. S9). GOx can decompose nutrients (glucose) to

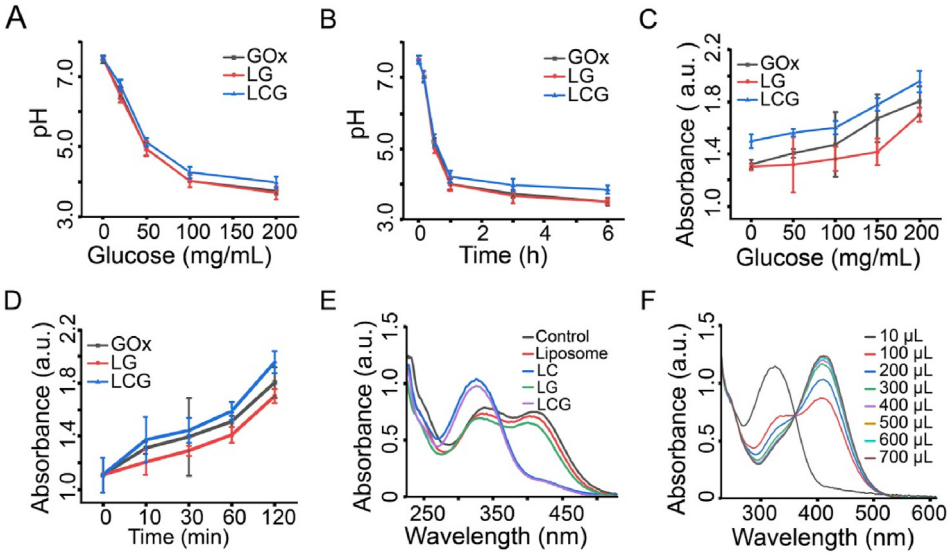

Figure 2 Multifaceted function tests in LCG including GOx enzymically-catalytic activity, H_2O_2 production and GSH depletion. (A) pH changes in GOX-, LG- or LCG-involved glucose solution with different glucose concentrations; (B) pH changes in GOX-, LG- or LCG-involved glucose solution at different periods. (C) Absorbance changes in H_2O_2 production by GOX, LG and LCG in glucose solution at different concentrations; and (D) Absorbance changes in H_2O_2 production by GOX, LG and LCG in glucose solution over time. (E) Absorbance changes in GSH content in solution after co-incubation of different materials with GSH (10 mmol/L); (F) Absorbance changes in GSH content in solution after co-incubation of different volumes of LCG with GSH (10 mmol/L). Data are expressed as mean ± SD (n = 3).

nourish tumor tissues, which inevitably competes with anaerobic glycolysis to consume glucose. It is well known that anaerobic glycolysis of glucose is responsible for LA production. As a result, LA production in LCG group, as anticipated, is significantly dampened (Fig. 3F), because LCG triggers the most glucose depletion and brings about the largest magnitude of H_2O_2 production (Fig. 3D). This result forebodes that LA-mediated immunosuppression will be removed. Regarding these, it is not difficult to understand why LCG induces the highest ROS level in 4T1 cells due to the presence of a proportional correlation between H_2O_2 concentration and ROS level (Fig. 3G). A lower pH value favors CaO_2 decomposition and boosts GOx activity to produce more H_2O_2 and decrease GSH (Fig. 2C−F), which eventually prefers to trigger more ROS production (Fig. 3G). As a general method, Ca^{2+} homeostasis disruption and glycometabolism interference enabled by LCG are also extended to act on other cell lines (H22) *by* producing abundant ROS (Supporting Information Fig. S10). The above inspiring results validate the remarkable cellular-level abilities of LCG including glucose depletion, H_2O_2 accumulation, GSH decrease, LA attenuation, pH decline, Ca^{2+} release and ROS enrichment (Scheme 1).

3.4. *In vitro anti-tumor test*

To investigate the anti-tumor ability of nanomaterials *in vitro*, cytotoxicity tests were conducted. Ca^{2+} homeostasis disruption and glycometabolism interference enable LCG to deplete glucose, produce H_2O_2 and ROS, attenuate GSH decrease and hamper LA birth, eventually tremendously killing 4T1 cells (Fig. 4A and B). Moreover, the killing effect exhibits concentration-dependent and time-dependent manners (Fig. 4A and B), wherein optimal concentration and incubation time can be determined. It is observed that the killing effect of Liposome liposomes alone on cells is negligible, indicating good biocompatibility and minimal impact on cells. To visually assess the therapeutic effect of LCG nanoparticles *in vitro*, propidium iodide (PI) was utilized to distinguish live and dead cells. The red fluorescence indicates that the number of dead cells is poor in the control and liposome groups. As a comparison, there is significantly higher number of dead cells with the strongest red fluorescence in the LCG treated group (Fig. 4C). Identical results are observed in H22 cells (Supporting Information Figs. S11 and S12), wherein LCG kill the most H22 cells as the functions of incubation time and LCG concentration. Furthermore, the potential of LCG to induce apoptosis was investigated. The number of LCG-induced apoptosis is much higher than that in LC- and LG-induced groups (Fig. 4D). To uncover the apoptosis percentage, co-staining with PI and annexin V-FITC of 4T1 cells was carried out after corresponding treatments in different groups, followed by FCM analysis. Almost all 4T1 cells in LCG group are dead, reaching 96.3% late apoptosis which is much higher than that in other groups (Fig. 4E).

Ca^{2+} homeostasis disruption by LCG was surveyed, and Ca^{2+} retention and distribution in 4T1 cells were first mapped using Fluo-4 AM as the indicator. After a 4-h co-incubation with nanoparticles, the cells were treated with Fluo-4 AM working solution to load the fluorescent probe. LCSM examination reveals that treatment with LC and LCG treatments significantly up-regulate the intracellular Ca^{2+} level in 4T1 cells (Fig. 4F and G). Considering that glycometabolism interference, ROS production and ion homeostasis disruption can induce ICD[11,19,44], we evaluated the effectiveness of LCG in inducing ICD by measuring typical markers such as adenosine triphosphate (ATP), calreticulin (CRT), HSP70 and high mobility group protein B1 (HMGB1). Compared with the control group, there is a dramatic decrease in intracellular ATP content within the cells after LCG treatment (Fig. 4H), suggesting energy supply blockade by GOx-mediated starvation therapy. The exposure of CRT on the surface of tumor cells is considered to be an "eat me" signal that recruits dendritic cells (DCs) to phagocytose tumor cells. Immunofluorescence

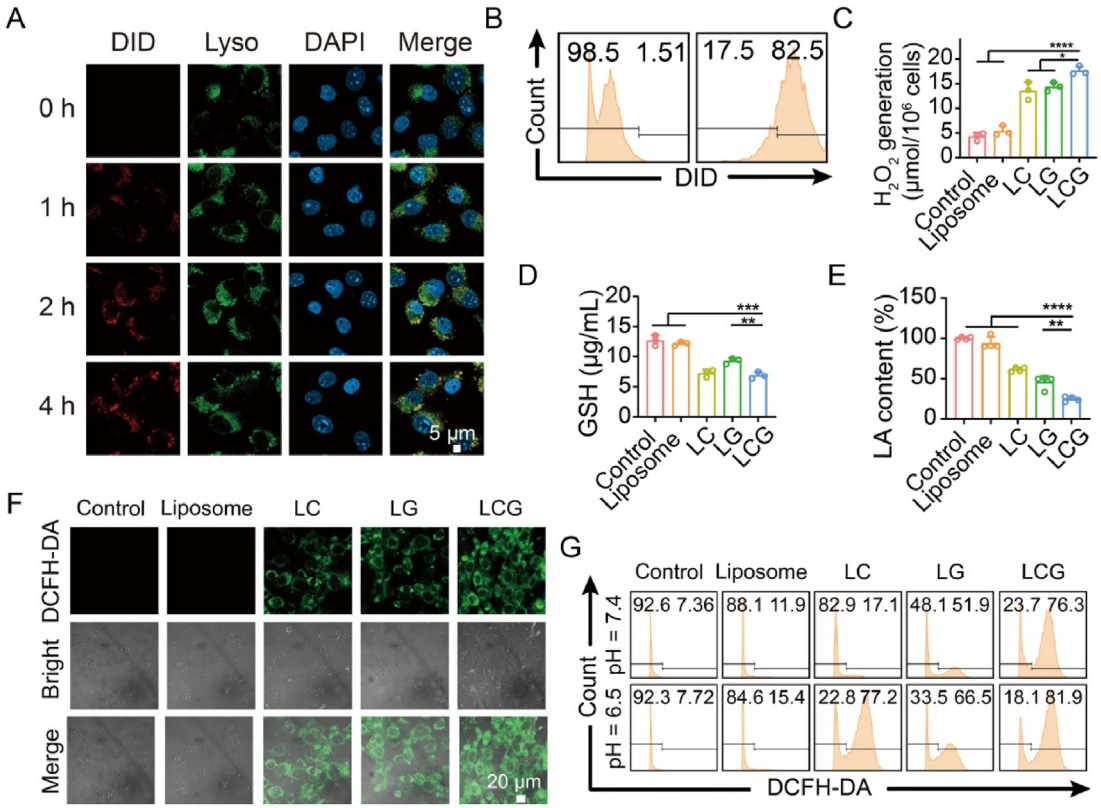

Figure 3 Cellular-level multifaceted events exploration and its role in promoting ROS production. (A) Fluorescence images of cells after different treatments (red fluorescence signal from LCG-DID, cells stained by DAPI and LysoTraker Green), scale bar = 5 μm; (B) FCM patterns of 4T1 cells after incubation with LCG-DID for different periods (0 and 4 h), both of which were used to assess the cellular phagocytosis of LCG-DID by 4T1 cells. (C) The concentration of Ca^{2+} in the culture medium following various cell treatments. (D–F) Intracellular contents of H_2O_2 (D), GSH (E) and LA (F) in 4T1 cells after co-incubation with different nanomaterials, scale bar = 20 μm; (G) CLSM images of 4T1 cells stained with DCFH-DA after co-incubation with different nanoparticles; and (H) FCM analysis of 4T1 cells stained with DCFH-DA after co-incubation with different nanoparticles, both of which could detect the intracellular ROS content after different treatments. Data are expressed as mean ± SD (n = 3); *P < 0.05, **P < 0.01, ***P < 0.001, ****P < 0.0001.

analysis and Western blot (WB) examination show no significant difference in CRT level between Liposome group and Control group in both 4T1 and H22 cells (Fig. 4I, L, O and Supporting Information Fig. S13), while the CRT level in the LCG-treated group is significantly higher than that in the control group (Fig. 4I, L, O and Fig. S13). Identical to CRT, LCG treatment regulates another hallmark of ICD, *i.e.*, HSP70, and brings about the highest HSP70 expression (Fig. 4J, M, O). Further, a notable reduction in the expression of intracellular HMGB1 means the efflux of HMGB1 secreted in nuclei to extracellular media (ECM)[45], which is also the typical event of ICD (Fig. 4K, N, O).

3.4.1. Anti-tumor effect

Before anti-tumor explorations, the entry and retention of LCG in 4T1 orthotopic tumor was investigated, where free DID or LCG-DID were administered tail vein injection and then time-dependent fluorescence imaging was carried out to map the distribution of DID or LGC-DID (Fig. 5A). Free DID fail to accumulate in tumor within 72 h, while LCG progressively enter and concentrate at the tumor site after 12 h post-injection. More significantly, the high accumulation can be maintained up to 72 h since fluorescence signal is still present at 72 h (Fig. 5B). The mouse heart, liver, spleen, lung, kidney, and tumor tissues were collected and observed at 6 h and 48 h. Compared to 6 h, fluorescence is only observed at the tumor site (Fig. 5C) and no evident fluorescence is observed in other normal tissues. This phenomenon suggests that LCG can be rapidly degraded in normal tissues, but can reside in the tumor tissues for an extended period. This merit is highly preferable for LCG to kill tumor cells effectively.

Anti-tumor experiments proceeded on the 4T1 mouse model (Fig. 5D). The change in body weight of mice is an important indicator for evaluating material biosafety. In the course of LCG treatment, mice in each group showed a consistent increase in body weight (Fig. 5E and Supporting Information Fig. S14). The mice in the PBS group exhibit a much higher rate of tumor growth compared to the other groups. Depending on the calcium homeostasis disruption- and glycometabolism interference-unlocked multifaceted actions, the LCG group receives the considerably-elevated inhibitory rate against tumor growth (Fig. 5F and Supporting Information Fig. S15). At the end of the treatment, tumors were extracted, weighed and photographed. The tumor weight of mice in the LCG group is the lowest (Fig. 5G and H), further verifying the excellent anti-tumor outcomes using LCG. To compare the tumor size before and after treatment, photographs were taken at two time points. It is evident that the tumors in the LCG group are significantly smaller than those in the PBS group (Fig. 5I). Furthermore, it is observed that mice in

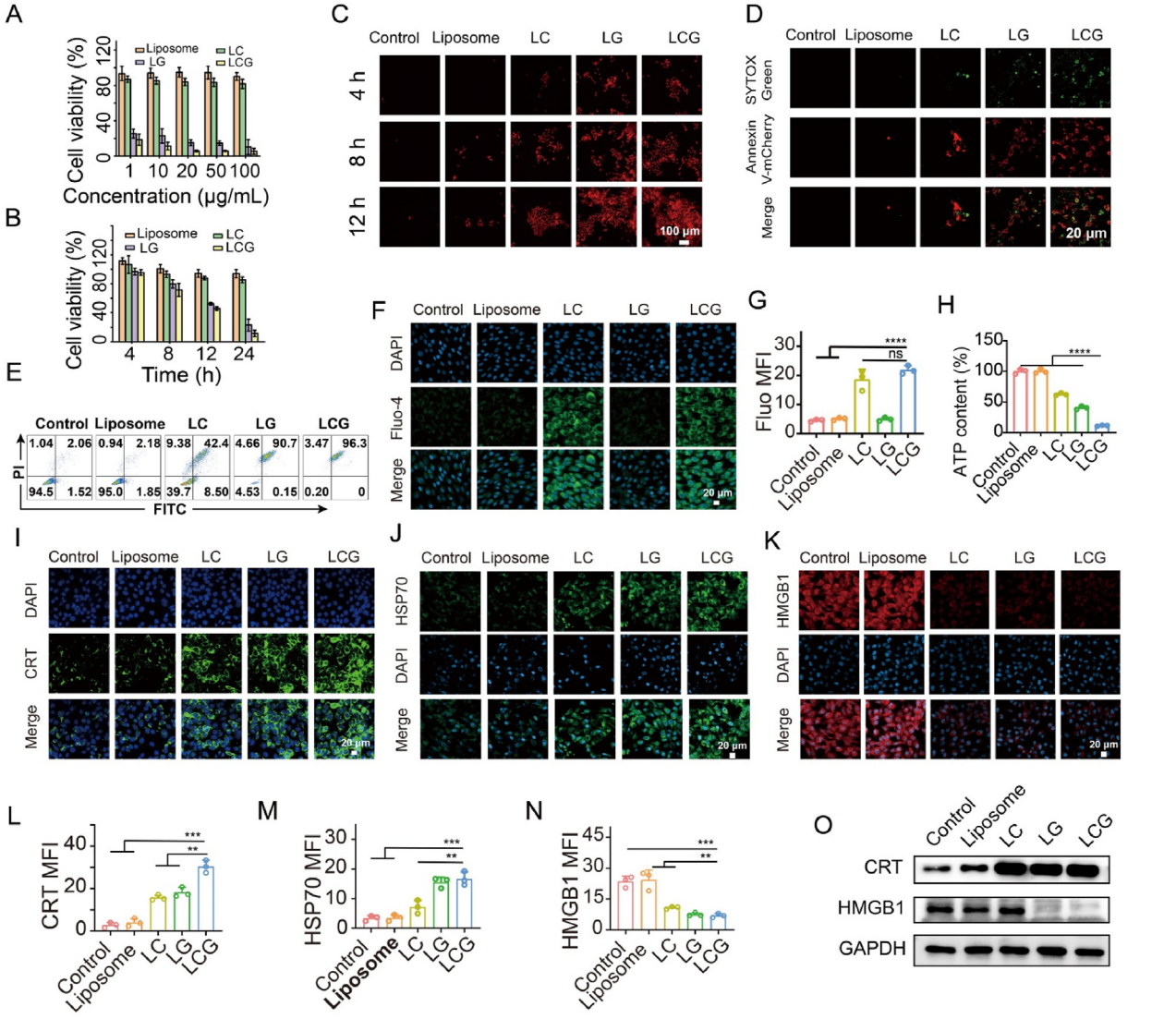

Figure 4 *In vitro* anti-tumor evaluations and cancer immunogenic death test. (A) Relative viability of 4T1 cells after incubations with different samples under varied concentrations for 24 h; (B) Relative viability of 4T1 cells after incubations with different samples under varied concentrations for different periods ($n = 6$); (C) CLSM images of PI-stained 4T1 cells in different experimental subgroups that experienced corresponding treatments for 4, 8 and 12 h, scale bar = 100 μm; (D) CLSM images of 4T1 cells co-stained with Annexin V-mCHerrry and SYTOX Green in different groups, scale bar = 20 μm; (E) FCM patterns of 4T1 cells stained with PI and Annexin V-FITC after co-incubation with different samples; (F) CLSM images of Fluo-4 AM-stained 4T1 cells after co-incubation with different nanoparticles for tracing intracellular Ca^{2+} levels, scale bar = 20 μm; and (G) corresponding MFI values. (H) Intracellular ATP content detection after co-incubation of 4T1 with different nanoparticles; (I−N) Immunofluorescence images (I−K) and corresponding MFI values (L−N) of CRT (I,L), HSP 70 (J, M) and HMGB1 (K, N), scale bar = 20 μm; (O) WB images of intracellular CRT and HMGB1 after different treatments. Data are expressed as mean ± SD ($n = 3$), 'ns' no significance, $^{**}P < 0.01$, $^{***}P < 0.001$ and $^{****}P < 0.0001$.

the LCG group exhibit a prolonged lifespan compared to those in other groups (Fig. 5J).

To figure out whether the anti-tumor outcome rely on the calcium homeostasis disruption and glycometabolism interference-enhanced ICD, the infiltration of T cells in tumors after different treatments was firstly traced. Our findings reveal a decrease in Tregs ($FOXP3^+CD4^+$) infiltration and an increase in $CD8^+$ T infiltration in the LCG treatment group compared to the control group (Fig. 5K, L and Supporting Information Fig. S16). This result uncovers that calcium homeostasis disruption and glycometabolism interference induced by LCG indeed enhance ICD to repress breast cancer through decomposing glucose, producing H_2O_2 and down-regulating GSH to enrich ROS and inhibiting LA birth (Fig. 5M and Supporting Information Fig. S17). Additionally, the pathological examination was carried out, where H&E staining of treated tumor tissues showed the lowest cell density and apoptosis of 4T1 cells in LCG group (Fig. 5N). Further, Ki67 and TUNEL that associated with proliferation and apoptosis of cells[38,46], were inspected after their corresponding immunohistochemical staining. As expected, LCG-treated tumors showed the lowest Ki67 expression and the highest TUNEL expression compared with other treatment groups (Fig. 5N and Supporting

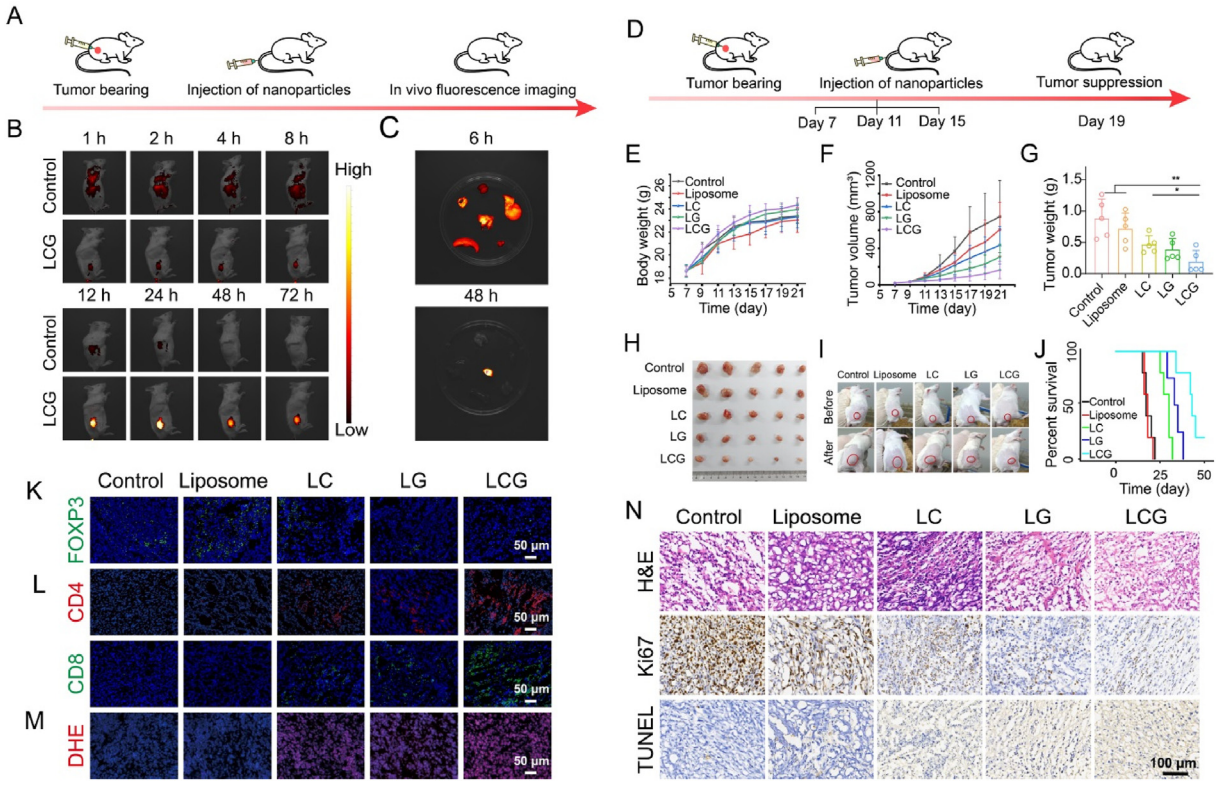

Figure 5 Anti-tumor assay and mechanism exploration. (A) Schematic of imaging in small animals; (B) Fluorescence biodistribution imaging of LCG in mice under different time points post-injection of LCG-DID and free DID (Control); (C) Fluorescence images of *vivo* organ harvested from LCG-treated mice after 6 and 48 h post-injection of LCG-DID. (D) Schematic diagram of tumors treated with different nanomaterials; (E) Time-dependent changes in the average body weight of mice in different treatment groups; (F) Time-dependent changes in the average tumor volume of mice in different treatment groups; (G) Time-dependent changes in the average tumor body weight in different treatment groups; (H) Digital images of excised tumors from mice in different treatment groups at the end of experiment period; (I) Photos of 4T1 tumor-bearing mice before and after different treatments in different treatment groups; (J) Survival rate of mice treated with various formulations in different treatment groups; (K) Immunofluorescence images of tumor slices co-stained with FOXP3 and DAPI after different treatments for assaying Tregs infiltration, scale bar = 50 μm; (L) Immunofluorescence images of tumor slices co-stained with CD4, CD8 and DAPI after different treatments for assaying T-cell infiltration, scale bar = 50 μm; (M) ROS levels in tumor sections stained with dihydroethidium (DHE), scale bar = 50 μm; (N) Optical photos of tumor slices after different immunochemical staining in different treatment groups for realizing H&E, KI67 and TUNEL expression analysis, scale bar = 50 μm. Data are expressed as mean ± SD ($n = 5$); $^{*}P < 0.05$ and $^{**}P < 0.01$.

Information Fig. S18). It indicates that the multifaceted actions in LCG can induce 4T1 apoptosis and hamper their expansion, which is responsible for the excellent anti-tumor consequences.

In order to investigate the biosafety of the synthesized nanomaterials, we conducted a study involving the removal of the heart, liver, spleen, lungs and kidneys from mice following various treatments. Tissue sections were then subjected to HE staining. No significant pathological changes are observed in the organs across different treatment groups (Supporting Information Fig. S19). Additionally, the hemolysis rate remains below 5%, indicating the excellent preservation of red blood cell integrity (Supporting Information Fig. S20). These findings demonstrate that our synthesized nanomaterials exhibit good biosafety and do not induce obvious adverse effects on the major organs of mice.

3.5. *Immune activation analysis*

We further investigated the role of LCG in inducing ICD and enhancing tumor immunity. ICD was assessed through monitoring the hallmark levels of ICD (CRT, HMGB1), and coincidently serum and tumor tissues were collected to evaluate cytokines and immune cells, respectively. Compared to either control or liposome alone, the CRT content in the LCG group is significantly increased (Fig. 6A and B), where the content of secreted HMGB1 in tumor tissues shows a similar rise trend since the HMGB1 ejected to ECM are also collected for analysis (Fig. 6A and C). Additionally, the intratumoral ATP level in the LCG-treated group is 5 times higher than that in the control or Liposome groups (Fig. 6D). These results confirm that LCG-treated group can boost ICD to activate robust immune responses.

The enzyme-linked immunosorbent assay (Elisa) results of serum in mice reveal the highest expression levels of interferon (IFN-γ) and anti-tumor cytokines (TNF-α and IL-6) in mice treated with LCG (Fig. 6E−G). These anti-tumor inflammatory factors are secreted by immune cells, thereby promising a robust immune response activation. To verify them, FCM was utilized to assess anti-tumor immune activation following different treatment methods. Results show that the control group and liposome group have a minimal impact on DCs maturation, while the LCG group receives a tremendously-increased maturation level of DCs (Fig. 6H and I). Subsequently, we examined the proportion of activated $CD8^{+}$ cells and Tregs in tumors after various treatments.

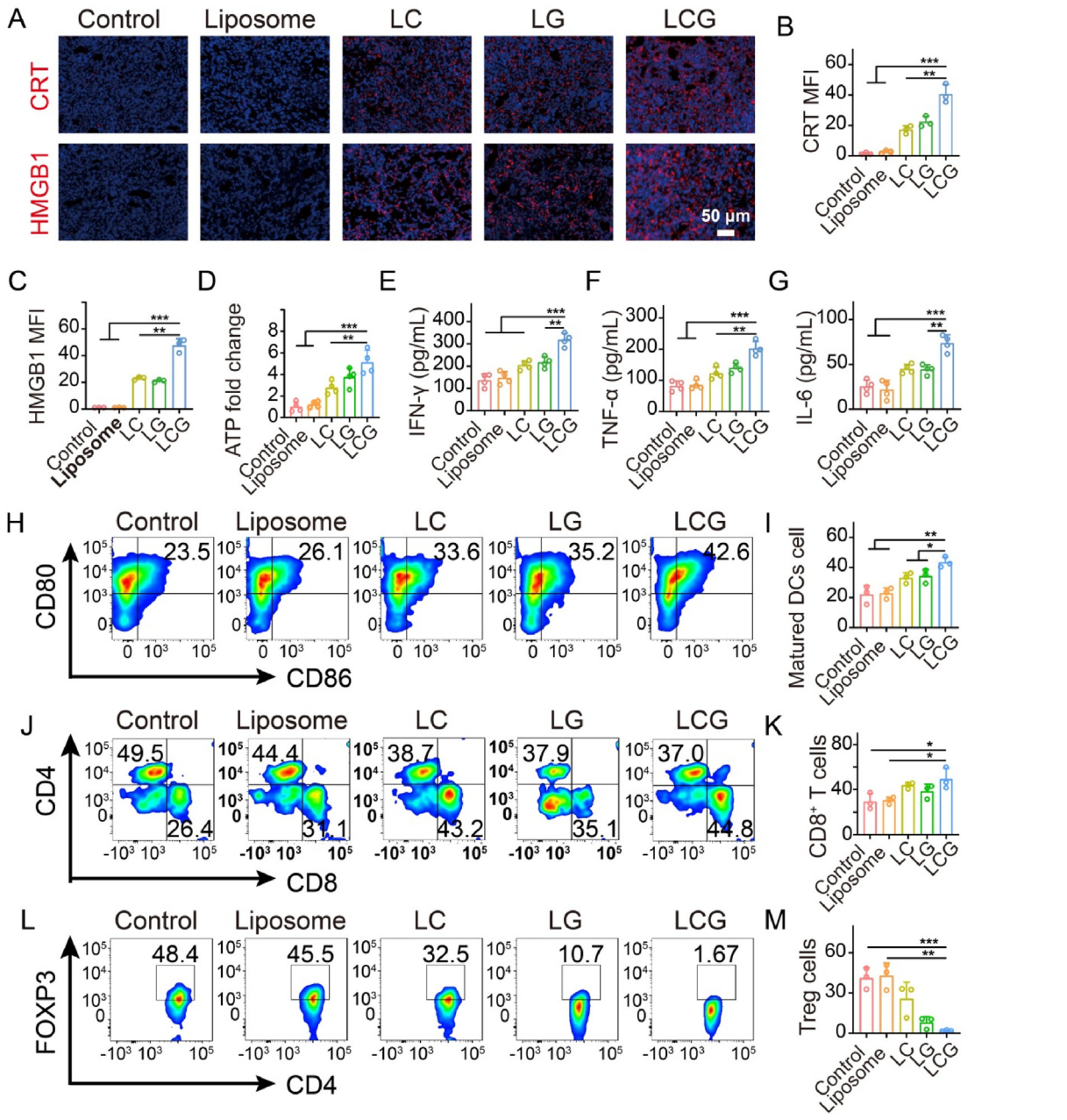

Figure 6 Induces ICD and activates immunity. (A−C) Fluorescence micrographs of 4T1 tumor tissue stained with CRT and HMGB1 (A), scale bar = 50 μm, along with the corresponding MFI (B,C); (D) Intratumoral ATP levels in tumor after different treatments (n = 4); (E−G) Secretion levels of IFN-γ (E), TNF-α (F), and IL-6 (G) in mouse serum based on Elisa kits (n = 4); (H,I) Representative FCM patterns (H) and quantitative analysis (I) of matured DCs ($CD80^+CD86^+$) in tumor tissues after various treatments; (J,K) Representative FCM patterns (J) and quantitative analysis (K) of $CD4^+$ and $CD8^+$ T cells in tumor tissues following various treatments (n = 3); (L, M) Representative FCM patterns (L) and quantitative analysis (M) of Tregs (($FOXP3^+CD4^+$) in tumor tissues following various treatments (n = 3). Data are expressed as mean ± SD; *P < 0.05, **P < 0.01 and ***P < 0.001.

It is found that the LCG treated group exhibits the highest proportion of $CD3^+CD8^+$T cells (47%), compared to 29% in the control group and 32% in the liposome group (Fig. 6J and K), respectively. Additionally, LCG group shows the lowest proportion of Tregs at 1.9% (Fig. 6L and M). These findings further confirm the powerful ability of LCG to activate anti-tumor immunity activation. The activated anti-tumor immune collaborated with another ability of LCG, LA inhibition-mediated immunosuppression attenuation, to magnify aforementioned anti-tumor outcomes of ion interference therapy and glycometabolism interference strategy in LCG.

4. Conclusions

In summary, we integrated a combined strategy consisting of calcium homeostasis disruption and glycometabolism interference into the LCG pharmaceutical loaded with GOx and CaO_2 so as to

address the complementary effects-associated tumor plasticity and resistance. The established LCG successfully decomposed glucose into H_2O_2, depleted GSH, competed with anaerobic glycolysis to hamper LA secretion, release Ca^{2+} and H_2O_2 and gave rise to abundant ROS, eventually achieving calcium homeostasis disruption and glycometabolism interference. Such multifaceted actions unlocked by calcium homeostasis disruption and glycometabolism interference in LCG impaired treatment resistance and plasticity of malignant breast cancer, enhanced cancer immunogenic deaths and coincidently opposed Tregs infiltration and promoted $CD8^+$ T recruitment. These contributions induced the apoptosis of breast cancer and suppressed breast cancer progression. Our findings provided adequate evidences that LCG was armed with the abilities to disrupt metabolic processes within the tumor microenvironment and establish an effective anti-tumor immune environment, holding high clinical translation potential.

Acknowledgments

This work was supported by Excellent Young Science Fund for National Natural Science Foundation of China (No. 82022033) and Sichuan Science and Technology Program (2024NSFJQ0048, China).

Author contributions

Qiuxia Peng: Writing − original draft, Visualization, Validation, Resources, Investigation, Formal analysis, Data curation. Xiaolong Li: Investigation, Funding acquisition, Formal analysis, Data curation. Chao Fang: Investigation, Formal analysis, Data curation. Chunyan Zhu: Formal analysis, Data curation. Taixia Wang: Investigation, Data curation. Binxu Yin: Resources, Investigation. Huaijuan Guo: Resources, Formal analysis. Yang Liu: Investigation. Kun Zhang: Writing − review & editing, Supervision, Project administration, Methodology, Funding acquisition, Formal analysis, Conceptualization.

Ethics approval and consent to participate

All animal experiments were conducted under the protocols approved by the Institutional Animal Care and Use Committee of Shanghai Tenth People's Hospital (approval No. SHDSYY-2022-7066). When the tumor volume of mice reached approximately 180 mm^3, mice carrying 4T1 tumors were randomly divided into five groups ($n = 5$) and injected with different nanomaterials. The mouse were eventually placed in a CO_2 chamber and the CO_2 concentration was gradually increased until respiratory cardiac arrest occurred.

Conflicts of interest

The authors declare that they have no competing interests.

Appendix A. Supporting information

Supporting information to this article can be found online at https://doi.org/10.1016/j.apsb.2024.12.018.

References

1. Siegel PM, Massagué J. Cytostatic and apoptotic actions of TGF-β in homeostasis and cancer. *Nat Rev Cancer* 2003;**3**:807−20.
2. DeBerardinis RJ, Chandel NS. Fundamentals of cancer metabolism. *Sci Adv* 2016;**2**:e1600200.
3. Panieri E, Santoro MM. ROS homeostasis and metabolism: a dangerous liaison in cancer cells. *Cell Death Dis* 2016;**7**:e2253.
4. Liu YY, Gu RJ, Gao MR, Wei YW, Shi Y, Wang X, et al. Emerging role of substance and energy metabolism associated with neuroendocrine regulation in tumor cells. *Front Endocrinol* 2023;**14**:1126271.
5. Zhang XN, Zhao Q, Yang JJ, Wang TX, Chen FB, Zhang K. Tumor microenvironment-triggered intratumoral *in-situ* biosynthesis of inorganic nanomaterials for precise tumor diagnostics. *Coord Chem Rev* 2023;**484**:215115.
6. Dong XL, Yang QL, Wang H, Zhu CY, Wang TX, Fang C, et al. Targetedly attenuating cancer stemness and plasticity by homologous cancer stem cell-inherited fusion membrane nanoeffectors against cancer metastasis. *Small Sci* 2024;**4**:2300111.
7. Bu ZT, Yang JJ, Zhang Y, Luo T, Fang C, Liang XY, et al. Sequential ubiquitination and phosphorylation epigenetics reshaping by MG132-loaded Fe-MOF disarms treatment resistance to repulse metastatic colorectal cancer. *Adv Sci* 2023;**10**:2301638.
8. Wang D, Zhu XQ, Wang XB, Wang Q, Yan KN, Zeng GC, et al. Multichannel sonocatalysis amplifiers target IDH1-mutated tumor plasticity and attenuate Ros tolerance to repress malignant cholangiocarcinoma. *Adv Funct Mater* 2023;**33**:2303869.
9. Vander Heiden MG, Cantley LC, Thompson CB. Understanding the Warburg effect: the metabolic requirements of cell proliferation. *Science* 2009;**324**:1029−33.
10. Liberti MV, Locasale JW. The warburg effect: how does it benefit cancer cells?. *Trends Biochem Sci* 2016;**41**:211−8.
11. Gao Y, Ouyang Z, Shen S, Yu H, Jia B, Wang H, et al. Manganese dioxide-entrapping dendrimers co-deliver protein and nucleotide for magnetic resonance imaging-guided chemodynamic/starvation/immune therapy of tumors. *ACS Nano* 2023;**17**:23889−902.
12. Zhang C, Han ZY, Chen KW, Wang YZ, Bao P, Ji P, et al. *In situ* formed microalgae-integrated living hydrogel for enhanced tumor starvation therapy and immunotherapy through photosynthetic oxygenation. *Nano Lett* 2024;**24**:3801−10.
13. Jiao R, Lin X, Zhang Q, Zhang Y, Qin W, Yang QL, et al. Anti-tumor immune potentiation targets-engineered nanobiotechnologies: design principles and applications. *Prog Mater Sci* 2024;**142**:101230.
14. Kumagai S, Koyama S, Itahashi K, Tanegashima T, Lin Y-T, Togashi Y, et al. Lactic acid promotes PD-1 expression in regulatory T cells in highly glycolytic tumor microenvironments. *Cancer Cell* 2022;**40**. 201-18.e9.
15. Watson MJ, Vignali PDA, Mullett SJ, Overacre-Delgoffe AE, Peralta RM, Grebinoski S, et al. Metabolic support of tumour-infiltrating regulatory T cells by lactic acid. *Nature* 2021;**591**:645−51.
16. Xu T, Hu J, Fang C, Luo T, Liu J, Zhang K. Composite hemostat spray seals post-surgical blood burst and ameliorates bacteria-arised inflammation for expediting wound healing. *ACS Mater Lett* 2023;**5**:1892−901.
17. Bose T, Cieslar-Pobuda A, Wiechec E. Role of ion channels in regulating Ca^{2+} homeostasis during the interplay between immune and cancer cells. *Cell Death Dis* 2015;**6**:e1648.
18. Feng Y, Liu Y, Ma X, Xu L, Ding D, Chen L, et al. Intracellular marriage of bicarbonate and Mn ions as "immune ion reactors" to regulate redox homeostasis and enhanced antitumor immune responses. *J Nanobiotechnol* 2022;**20**:193.
19. Chen Z, Guo W, Tan L, Fu C, Wu Q, Ren X, et al. Biomimetic MOF-based nano-immunoactivator *via* disruption of ion homeostasis for strengthened tumor microwave-immunotherapy. *Adv Funct Mater* 2024;**34**:2401359.
20. Qian R, Yi X, Liu T, Chen H, Wang Y, Hu L, et al. Regulation of ion homeostasis for enhanced tumor radio-immunotherapy. *Adv Sci* 2023;**10**:2304092.
21. Liu Y, Zhang M, Bu W. Bioactive nanomaterials for ion-interference therapy. *View* 2020;**1**:e18.
22. Zhuang H, He X, Li H, Chen Y, Wu T, Jiang X, et al. MnS nanocapsule mediates mitochondrial membrane permeability transition for tumor ion-interference therapy. *ACS Nano* 2023;**17**:13872−84.

23. Ge JC, Fang C, Tan HS, Zhan M, Gu M, Ni JS, et al. Endogenous Zinc-ion-triggered *in situ* gelation enables Zn capture to reprogram benign hyperplastic prostate microenvironment and shrink prostate. *Adv Mater* 2024;**36**:2307796.
24. Liang X, Zhang Y, Zhou J, Bu Z, Liu J, Zhang K. Tumor microenvironment-triggered intratumoral *in situ* construction of theranostic supramolecular self-assembly. *Coord Chem Rev* 2022;**473**:214824.
25. Fu LH, Qi C, Hu YR, Lin J, Huang P. Glucose oxidase-instructed multimodal synergistic cancer therapy. *Adv Mater* 2019;**31**:1808325.
26. Xu Y, Liu SY, Zeng L, Ma H, Zhang Y, Yang H, et al. An enzyme-engineered nonporous copper (I) coordination polymer nanoplatform for cuproptosis-based synergistic cancer therapy. *Adv Mater* 2022;**34**:2204733.
27. Li S, Jiang Q, Liu S, Zhang Y, Tian Y, Song C, et al. A DNA nanorobot functions as a cancer therapeutic in response to a molecular trigger *in vivo*. *Nat Biotechnol* 2018;**36**:258−64.
28. Zhang K, Fang Y, He Y, Yin H, Guan X, Pu Y, et al. Extravascular gelation shrinkage-derived internal stress enables tumor starvation therapy with suppressed metastasis and recurrence. *Nat Commun* 2019;**10**:5380.
29. He Y, Wang T, Song Y, Fang C, Wang Y, Dong X, et al. Targeting vascular destruction by sonosensitizer-free sonocatalytic nanomissiles instigates thrombus aggregation and nutrition deprivation to starve pancreatic cancer. *Adv Funct Mater* 2024;**34**:2315394.
30. Zhou J, Li M, Hou Y, Luo Z, Chen Q, Cao H, et al. Engineering of a nanosized biocatalyst for combined tumor starvation and low-temperature photothermal therapy. *ACS Nano* 2018;**12**:2858−72.
31. Fan WP, Lu N, Huang P, Liu Y, Yang Z, Wang S, et al. Glucose-responsive sequential generation of hydrogen peroxide and nitric oxide for synergistic cancer starving-like/gas therapy. *Angew Chem-Int Edit* 2017;**56**:1229−33.
32. Gu J, Zhou J, Chen Q, Xu X, Gao J, Li X, et al. Tumor metabolite lactate promotes tumorigenesis by modulating MOESIN lactylation and enhancing TGF-β signaling in regulatory T cells. *Cell Rep* 2022;**39**:110986.
33. Zhang M, Song R, Liu Y, Yi Z, Meng X, Zhang J, et al. Calcium-overload-mediated tumor therapy by calcium peroxide nanoparticles. *Chem* 2019;**5**:2171−82.
34. Li W, Yang J, Luo L, Jiang M, Qin B, Yin H, et al. Targeting photodynamic and photothermal therapy to the endoplasmic reticulum enhances immunogenic cancer cell death. *Nat Commun* 2019;**10**:3349.
35. Cao D, Guo W, Cai C, Tang J, Rao W, Wang Y, et al. Unified therapeutic-prophylactic vaccine demonstrated with a postoperative filler gel to prevent tumor recurrence and metastasis. *Adv Funct Mater* 2022;**32**:2206084.
36. Zhang Y, Fang C, Zhang W, Zhang K. Emerging pyroptosis-engineered nanobiotechnologies regulate cancers and inflammatory diseases: a double-edged sword. *Matter* 2022;**5**:3740−74.
37. Qin W, Yang Q, Zhu C, Jiao R, Lin X, Fang C, et al. A distinctive insight into inorganic sonosensitizers: design principles and application domains. *Small* 2024;**20**:2311228.
38. Wang D, Zhang MQ, Zhang Y, Qiu GH, Chen J, Zhu XQ, et al. Intraparticle double-scattering-decoded sonogenetics for augmenting immune checkpoint blockade and CAR-T therapy. *Adv Sci* 2022;**9**:2203106.
39. Shen S, Mamat M, Zhang S, Cao J, Hood ZD, Figueroa-Cosme L, et al. Synthesis of CaO_2 nanocrystals and their spherical aggregates with uniform sizes for use as a biodegradable bacteriostatic agent. *Small* 2019;**15**:1902118.
40. Khodaveisi J, Banejad H, Afkhami A, Olyaie E, Lashgari S, Dashti R. Synthesis of calcium peroxide nanoparticles as an innovative reagent for *in situ* chemical oxidation. *J Hazard Mater* 2011;**192**:1437−40.
41. He C, Zhang S, Liu X, Wang J, Huang Y, Zhang A, et al. CaO_2 nanomedicines: a review of their emerging roles in cancer therapy. *Nanotechnology* 2023;**34**:482002.
42. Wang Z, Liu B, Sun Q, Dong S, Kuang Y, Dong Y, et al. Fusiform-like Copper(II)-based metal-organic framework through relief hypoxia and GSH-depletion co-enhanced starvation and chemodynamic synergetic cancer therapy. *ACS Appl Mater Inter* 2020;**12**:17254−67.
43. Fitri LE, Sardjono TW, Simamora D, Sumarno Setyawati SK. High dose of *N*-acetylcysteine increase H_2O_2 and MDA levels and decrease GSH level of HUVECs exposed with malaria serum. *Trop Biomed* 2011;**28**:7−15.
44. Kong FL, Fang C, Zhang Y, Duan LX, Du D, Xu G, et al. Abundance and metabolism disruptions of intratumoral microbiota by chemical and physical actions unfreeze tumor treatment resistance. *Adv Sci* 2022;**9**:2105523.
45. Deng H, Yang W, Zhou Z, Tian R, Lin L, Ma Y, et al. Targeted scavenging of extracellular ROS relieves suppressive immunogenic cell death. *Nat Commun* 2020;**11**:4951.
46. Zhou H, Zhu C, Zhao Q, Ni J, Zhang H, Yang G, et al. Wrecking neutrophil extracellular traps and antagonizing cancer-associated neurotransmitters by interpenetrating network hydrogels prevent post-surgical cancer relapse and metastases. *Bioact Mater* 2024;**39**:14−24.